Nonlocal pseudopotential energy density functional for semiconductors

Cheng Ma,[1,2] Qiang Xu,[1] Wenhui Mi,[1,2,3,*] Yanchao Wang,[1,2,†] and Yanming Ma[1,2,3,‡]
[1]*Key Laboratory of Material Simulation Methods & Software of Ministry of Education, College of Physics, Jilin University, Changchun 130012, China*
[2]*State Key Lab of Superhard Materials, College of Physics, Jilin University, Changchun 130012, China*
[3]*International Center of Future Science, Jilin University, Changchun 130012, China*

(Received 5 September 2023; revised 3 January 2024; accepted 25 January 2024; published 21 February 2024)

Due to the linear scaling of the computational cost with system size, orbital-free density functional theory (OF-DFT) offers a promising approach for large-scale materials simulations. However, the lack of high transferability local pseudopotentials in OF-DFT has impeded its wide use for materials simulations. Recently, the nonlocal pseudopotential energy density functional (NLPPF) method [Nat. Commun. **13**, 1385 (2022)] has been proposed to enable OF-DFT to directly use nonlocal pseudopotentials and successfully applied to simple metallic systems formed by *sp*-block metallic elements. Here, we extend the NLPPF scheme for applications to the semiconducting systems by employment of the revised Huang-Carter kinetic-energy density functional. Applications of typical semiconductors including Si, Ge, and GaAs have systematically benchmarked the scheme. The results demonstrate that the NLPPF scheme combined with the revised Huang-Carter kinetic-energy density functional can significantly improve the accuracy of OF-DFT for simulating the semiconductors without extensive requirements of computational budget, which opens up new opportunities for OF-DFT applications to large-scale semiconducting systems.

DOI: 10.1103/PhysRevB.109.075144

I. INTRODUCTION

The large-scale simulations from an atomistic viewpoint play a significant role in understanding many physics aspects over wide spatiotemporal scales. Particularly, Kohn-Sham density functional theory (KS-DFT) [1,2] has been widely employed to describe the fundamental properties of various materials due to its good compromise between accuracy and computational cost. However, the computational cost of KS-DFT often scales cubically with the number of atoms in the simulated cell [3]. Even with enormous computing power, the KS-DFT is usually limited to a few thousand atoms, which is tiny compared with real systems. Furthermore, regarding simulation time, KS-DFT is limited to a few picoseconds, much shorter than experimental measurements [4]. Therefore, many problems at the leading edge of materials science involving large length and long time scale simulations are intrinsically challenging to access using conventional KS-DFT.

As an alternative DFT approach, orbital-free density functional theory (OF-DFT) uses the electron density as the sole variable to calculate total energies [5–7] and has been significantly advanced in the past decades [8–13]. In contrast with KS-DFT, the intrinsic linear scaling of OF-DFT with low prefactor [13–16] provides an ideal opportunity to understand many real behaviors (e.g., crystal growth processes [17,18]) of complex materials of interest [14]. Currently, a large number of OF-DFT methods and codes (e.g., PROFESS [19], GPAW [20], DFT-FE [21], DFTpy [22], CONUNDrum [23], and ATLAS [16,24]) have been developed and successfully applied to the systems containing millions of atoms [22,24–26]. From this viewpoint, these methods and codes become fascinating platforms that can be applied to large-scale systems with moderate computational cost.

It is well known that the reliability of OF-DFT simulations relies mainly on the qualities of the noninteracting kinetic energy and the electron-ion (or electron-pseudocore) interaction energy. The former is usually estimated by the kinetic-energy density functionals (KEDFs) [27–40]. Currently, several KEDFs, including WT [28], WGC [31,32], XWM [33], HC [35,41], LMGP [34,42], LDAK [36], and revHC [37] have been proposed and successfully applied to some metallic or semiconducting systems. At the same time, the local pseudopotentials (LPPs) were typically adopted for calculating electron-ion interaction energy in the OF-DFT simulations [43–49]. Despite some LPPs [e.g., the bulk-derived local pseudopotential(BLPS) [43,44], optimal effective local pseudopotential [45] (OEPP), and globally optimized local pseudopotential [46] (goLPS)] have been available, these LPPs usually suffer from a lack of transferability and sufficient accuracy, since they fail to reproduce the correct scattering behavior of the all-electron potentials.

Two frameworks of OF-DFT, including angular-momentum-dependent OF-DFT [50,51] and the nonlocal pseudopotential energy density functional (NLPPF) [52] have been proposed to include the critically important effects of nonlocal interactions. Particularly, the NLPPF scheme developed based on XWM or WT KEDFs significantly

*mwh@jlu.edu.cn
†wyc@calypso.cn
‡mym@jlu.edu.cn

improves the computational accuracy for *s*- and *p*-block metals over LPPs. These KEDFs, however, have proven to be not suitable for semiconducting systems. Here, we further extend the NLPPF for applications of semiconducting systems by employment of the revHC KEDF, which is suitable for semiconductors. The accuracy and efficiency of the NLPPF scheme have been benchmarked by comparisons against the KS-DFT calculations. The results demonstrate that the NLPPF within revHC KEDF can accurately reproduce the bulk properties of KS-DFT for bulk Si and III-V compounds, opening up new opportunities for applications of OF-DFT for simulations of large-scale semiconductors.

The reminder of this paper is organized as follows: Section II gives detailed information of the NLPPF scheme for the electron-ion interaction energy calculation for semiconductors. The computational details are provided in Sec. III. The results and discussions of NLPPF for simulations of bulk properties are illustrated in Sec. IV, followed by the conclusions in Sec. V.

II. METHODS

For the sake of clarity, we first briefly sketched the NLPPF scheme, in which the total energy of the considered system as functional of the electron-density function $\rho(\mathbf{r})$ can be formulated as

$$E[\rho] = T_s[\rho] + E_{\mathrm{H}}[\rho] + E_{XC}[\rho] + E_{II}(\{R_a\}) + \underbrace{E_{\mathrm{loc}}[\rho] + E_{\mathrm{nl}}[\rho]}_{E_{EI}[\rho]}, \tag{1}$$

where $T_s[\rho]$, $E_H[\rho]$, $E_{XC}[\rho]$, $E_{II}(\{R_a\})$, and $E_{EI}[\rho]$ are terms of noninteracting kinetic energy, the Hartree energy, the exchange-correlation energy, the ion-ion repulsion energy, and the electron-ion interaction energy, respectively. The electron-ion interaction energy can be further separated into two parts: local part $E_{\mathrm{loc}}[\rho] = \int \rho(\mathbf{r}) V_{\mathrm{loc}}(\mathbf{r}) d^3\mathbf{r}$ and nonlocal part $E_{\mathrm{nl}}[\rho]$. Note that the local part of the pseudopotential can be evaluated easily. While the exact nonlocal electron-ion interaction energy depends on the density matrix as [52]

$$E_{\mathrm{nl}}[\rho] = \iint V_{\mathrm{nl}}(\mathbf{r}, \mathbf{r}')\gamma_s(\mathbf{r}', \mathbf{r}) d\mathbf{r} d\mathbf{r}', \tag{2}$$

where $V_{\mathrm{nl}}(\mathbf{r}, \mathbf{r}') = \langle \mathbf{r}|\hat{V}_{\mathrm{nl}}|\mathbf{r}'\rangle$ and $\gamma_s(\mathbf{r}', \mathbf{r}) = \sum_i f_i \psi_i(\mathbf{r}')\psi_i^*(\mathbf{r})$ represent real-space representation of the nonlocal part pseudopotential and noninteracting density matrix. Note that f_i and $\psi_i(\mathbf{r})$ denote the occupation number and Kohn-Sham orbital, respectively.

In the NLPPF scheme, the nonlocal electron-ion interaction energy is treated as a functional of electron density:

$$E_{\mathrm{nl}}[\rho] = \iint V_{\mathrm{nl}}(\mathbf{r}, \mathbf{r}')\gamma_s[\rho](\mathbf{r}', \mathbf{r}) d\mathbf{r} d\mathbf{r}'. \tag{3}$$

The Kleinman-Bylander form [53] of norm-conserving nonlocal pseudopotentials (NLPPs) [54] was used to evaluate the nonlocal electron-ion interaction energy [52]. Specifically, the nonlocal part of the pseudopotential is defined as $V_{\mathrm{nl}}(\mathbf{r}, \mathbf{r}') = \sum_{a,lm} E_{KB}^{a,lm} \chi_{lm}^a(|\mathbf{R}_a - \mathbf{r}|)\chi_{lm}^{a*}(|\mathbf{R}_a - \mathbf{r}'|)$, where $E_{KB}^{a,lm} = [\int \phi_{lm}^{a*}(\mathbf{r})\delta V_{lm}^a(\mathbf{r})\phi_{lm}^a(\mathbf{r}) d\mathbf{r}]^{-1}$ and $\chi_{lm}^a(\mathbf{r}) = \delta V_{lm}^a(\mathbf{r})\phi_{lm}^a(\mathbf{r})$. Here, $\phi_{lm}^a(\mathbf{r})$ and $\delta V_{lm}^a(\mathbf{r})$ are the atomic pseudo wave function and the short-range pseudopotential within the cutoff radius associated with the lmth angular momentum of the ath atom.

In our scheme, the density matrix of $\gamma_s[\rho](\mathbf{r}', \mathbf{r})$ can be approximated explicitly as a functional of electron density, deriving from the modified Gaussian [55] density-matrix functional $\gamma_s^{MG}(\bar{\mathbf{r}}, s)$:

$$\gamma_s^{MG}(\bar{\mathbf{r}}, s) = \rho(\bar{\mathbf{r}}) e^{\frac{-s^2}{\beta(\bar{\mathbf{r}})}} \left[1 + A\left(\frac{s^2}{\beta(\bar{\mathbf{r}})}\right)^2\right]. \tag{4}$$

This expression is derived through a second-order Taylor expansion of the exact density matrix at $s = 0$, given by $\gamma(\bar{\mathbf{r}}, s) = \rho(\bar{\mathbf{r}})[1 - s^2/\beta(\bar{\mathbf{r}}) + O(s^4)]$. Here, $\bar{\mathbf{r}} = \frac{\mathbf{r}+\mathbf{r}'}{2}$, and $s = |\mathbf{r} - \mathbf{r}'|$. The parameter $\beta(\mathbf{r}) = (3/2)[\rho(\mathbf{r})/\tau_s(\mathbf{r})]$ is referred to as the "local temperature" [56,57], where $\tau_s(\mathbf{r})$ represents the kinetic-energy density (KED) [56]. Practically, the KED can be derived from the KEDF.

Previously, the WT and XWM KEDFs have been utilized in constructing NLPPFs for simulations involving *s*- and *p*-block metals [52]. In this work, the revHC functional, well-suited for semiconductors [37], is adopted as the KEDF, and its KED is employed in constructing the NLPPF. The revHC KEDF can be expressed as

$$T_s^{\mathrm{revHC}}[\rho] = T_s^{\mathrm{TF}}[\rho] + T_s^{\mathrm{vW}}[\rho] + T_s^{\mathrm{NL}}[\rho], \tag{5}$$

where $T_s^{\mathrm{TF}}[\rho] = C_{\mathrm{TF}} \int \rho^{\frac{5}{3}}(\mathbf{r}) d\mathbf{r}$ and $T_s^{\mathrm{vW}}[\rho] = \frac{1}{8} \int \frac{|\nabla\rho(\mathbf{r})|^2}{\rho(\mathbf{r})} d\mathbf{r}$ represent the of Thomas-Fermi (TF) [5,6] and von Weizsäcker (vW) [7] KEDF, respectively. $C_{\mathrm{TF}} = (3/10)(3\pi^2)^{\frac{2}{3}}$ is the Thomas-Fermi constant.

The nonlocal term $T_s^{\mathrm{NL}}[\rho]$ of the revHC KEDF can be written as

$$T_s^{\mathrm{NL}}[\rho] = \iint \rho^2(\mathbf{r})\omega[\xi(\mathbf{r})|\mathbf{r} - \mathbf{r}'|]\rho^{\frac{2}{3}}(\mathbf{r}') d\mathbf{r} d\mathbf{r}', \tag{6}$$

where $\xi(\mathbf{r})$ is the single-point density-dependent approximated effective Fermi wave vector in revHC KEDF [37],

$$\xi(\mathbf{r}) = k_{\mathrm{F}}(\mathbf{r})\left[1 + \frac{as^2(\mathbf{r})}{1 + bs^2(\mathbf{r})}\right]. \tag{7}$$

Here, $k_F(\mathbf{r}) = [3\pi^2\rho(\mathbf{r})]^{\frac{1}{3}}$ and $s(\mathbf{r}) = |\nabla\rho(\mathbf{r})|/[2(3\pi^2)^{\frac{1}{3}}\rho^{\frac{4}{3}}(\mathbf{r})]$ are the Fermi vector and the dimensionless reduced density gradient, respectively. The parameters of a and b are set as the same with original revHC KEDF [37]. The detailed derivations of revHC KEDF can be found in Refs. [35,37]. For the TF and vW term, the KED can be expressed as $\tau_s^{\mathrm{TF}}(\mathbf{r}) = C_{\mathrm{TF}}\rho^{\frac{5}{3}}(\mathbf{r})$ and $\tau_s^{\mathrm{vW}}(\mathbf{r}) = (1/8)[|\nabla\rho(\mathbf{r})|^2/\rho(\mathbf{r})]$, respectively. Regarding the nonlocal term $T_s^{\mathrm{NL}}[\rho]$ with double integral, there are two natural ways to define the KED with different local coordinates:

$$\tau_s^{\mathrm{NL}(\alpha)}(\mathbf{r}) = \rho^2(\mathbf{r}) \int \omega[\xi(\mathbf{r})|\mathbf{r} - \mathbf{r}'|]\rho^{\frac{2}{3}}(\mathbf{r}') d\mathbf{r}', \tag{8}$$

$$\tau_s^{\mathrm{NL}(\beta)}(\mathbf{r}) = \rho^{\frac{2}{3}}(\mathbf{r}) \int \omega[\xi(\mathbf{r}')|\mathbf{r} - \mathbf{r}'|]\rho^2(\mathbf{r}') d\mathbf{r}'. \tag{9}$$

Hence, the KED can also be expressed as a linear combination of these two definitions, i.e., $\tau_s^{\mathrm{NL}}(\mathbf{r}) = \lambda\tau_s^{\mathrm{NL}(\alpha)}(\mathbf{r}) + (1 - \lambda)\tau_s^{\mathrm{NL}(\beta)}(\mathbf{r})$. In line with previous work [52,58], we adopt the simple average definition with $\lambda = 1/2$.

TABLE I. Parameters for the electron configurations, cutoff radius r_c used in FHI98PP [73] for generation of TM-NLPP [72], and the parameters of A and q employed in NLPPF [52] for OF-DFT calculations. Note that only s and p channels were included within the NLPPF framework, due to the negligible occupation number of d channel for sp-block elements.

Element	Configuration	$r_c(s, p, d)$	A	q
Si	$3s^2 3p^2$	2.20, 2.20, 2.02	−1.8	−1.0
Ge	$4s^2 4p^2$	1.98, 2.18, 2.46	0.9	−0.1
Ga	$4s^2 4p^1$	2.30, 2.30, 2.80	0.3	−1.0
As	$4s^2 4p^3$	2.30, 1.90, 2.30	−2.0	−1.0
C	$2s^2 2p^2$	1.50, 1.50, -	−2.0	−1.0

To simplify the density matrix, we approximate $\rho(\bar{\mathbf{r}})$ as

$$\rho_q(\mathbf{r}', \mathbf{r}) = \left[\frac{\rho^q(\mathbf{r}') + \rho^q(\mathbf{r})}{2}\right]^{\frac{1}{q}}$$

and $\beta(\bar{\mathbf{r}})$ as

$$\beta(\mathbf{r}', \mathbf{r}) = \frac{\beta(\mathbf{r}') + \beta(\mathbf{r})}{2}.$$

Here, $\beta(\mathbf{r}', \mathbf{r})$ denotes the q-mean "nonlocal density," and $\beta(\mathbf{r}', \mathbf{r})$ is the two-point average temperature. The density matrix can then be reformulated as

$$\tilde{\gamma}_s^{MG}[\rho](\mathbf{r}', \mathbf{r}) = \rho_q(\mathbf{r}', \mathbf{r}) e^{-\frac{|\mathbf{r}'-\mathbf{r}|^2}{2\beta(\mathbf{r}', \mathbf{r})}} \left[1 + A\left(\frac{|\mathbf{r}' - \mathbf{r}|^2}{2\beta(\mathbf{r}', \mathbf{r})}\right)^2\right]. \tag{10}$$

The parameters A and q within the NLPPF are determined by fitting against solid properties estimated by KS-DFT and OF-DFT. Despite being derived from data fitting, these parameters are element-dependent and exhibit good transferability, since the density matrix is constrained to short-range, localized regions that near the atomic nuclei. By combining Eqs. (3) and (10), the NLPPF can be formally expressed as

$$E_{\text{nl}}[\rho] = \sum_{a,lm} E_{KB}^{a,lm} \int_{\Omega_a}\int_{\Omega_a} \chi_{lm}^a(|\mathbf{R}_a - \mathbf{r}|)\tilde{\gamma}_s^{MG}[\rho](\mathbf{r}, \mathbf{r}') \times \chi_{lm}^a(|\mathbf{R}_a - \mathbf{r}'|) d\mathbf{r} d\mathbf{r}'. \tag{11}$$

Here, the integral domain Ω_a corresponds to the ionic core region of the ath atom. Due to the short-range characteristics of $\chi_{lm}^a(|\mathbf{R}_a - \mathbf{r}|)$, the computational cost of NLPPF scales linearly with the number of atoms. The details of functional derivatives and implementation of revHC KEDF and NLPPF in ATLAS [16,24] were provided in the Supplemental Material [71].

III. COMPUTATIONAL DETAILS

All the OF-DFT calculations were performed by ATLAS 3.0 [16,24]. The Troullier-Martins NLPPs [72] generated by FHI98PP [73] and the detailed electron configuration parameters and cutoff radius for generating NLPPs for Si, Ge, As, Ga, and C were presented in Table I. Note that the OF-DFT calculations of Si, As, Ga, C, and GaAs were performed by using the BLPSs [43,44], while the OEPP [45] was adopted for Ge. The grid spacings of 0.08 and 0.10 Å have been used for bulk Si and other systems to ensure an energy convergence of better than 5 meV/atom, respectively. The energy densities including KED and nonlocal electron-ion interaction energy density were obtained by non-self-consistent calculations, where a finer grid spacing of 0.06 Å was employed. The parameters A and q in NLPPF for all OF-DFT calculations were also outlined in Table I. The OE-SCF solver [74] was adopted for the computational efficiency test.

The KS-DFT calculations have been performed by VASP 6.1.0 [75,76], CASTEP 8.0 [77], and ARES 1.0 [78], where the projector augmented-wave potentials (PAW) [79] and NLPPs have been employed to calculate the electron-ion interaction energy. The k-point meshes used in VASP, CASTEP, and ARES have been generated using the Monkhorst-Pack method [80] with a k spacing of 0.10, 0.016, and 0.14 Å^{-1}, respectively. The kinetic-energy cutoffs of 600 and 1000 eV were adopted in VASP and CASTEP for KS-DFT simulations, respectively. The same grid spacings were used for ARES and OF-DFT calculations. In all KS-DFT and OF-DFT calculations, the generalized gradient approximation with the Perdew-Burke-Ernzerhof [81,82] form was employed for electron exchange-correlation energy.

IV. RESULTS AND DISCUSSION

A. Bulk properties of semiconductors

Our previous results have shown that the NLPPF scheme within WT [28] and XWM [33] KEDFs gives comparable quantitatively accurate simulations for nearly-free-electron-like main group metals (e.g., Li, Mg, and Cs) to KS-DFT. Particularly, it significantly improves the computational accuracy and transferability over conventional LPP for crystalline Be [52]. To assess the accuracy of the scheme for semiconductors, we first apply it to investigate the bulk properties of Si with several prototype phases [43] including the cubic diamond (CD), hexagonal diamond (HD), complex body-centered-cubic (CBCC), β-tin, body-centered-tetragonal 5 (BCT5) [83], simple-cubic (SC), hexagonal-close-packed (HCP), body-centered-cubic (BCC), and face-centered-cubic (FCC) structures [84]. Note that the bulk properties of bulk modulus (B_0), equilibrium volumes (V_0), and relative energy with respect to the selected reference structure (E_R) are obtained by expanding and compressing the KS-DFT equilibrium unit cell structure up to 20% with 15 points and fitting the energy curves versus volume against Murnaghan's equation of state [85].

The high-quality LPPs of both BLPSs [43,44] and OEPPs [45] have been demonstrated by successful reproduction of the bulk properties for the most of groups III–V p-block elements (e.g., Si, Ga, and As) [35,37]. Therefore, we expect the NLPPF scheme to be equally accurate as the LPPs for systems composed of these elements. The accuracy of the NLPPF scheme is demonstrated through direct comparisons of bulk properties (e.g., E_R, V_0, and B_0) to results from KS-DFT with the PAW method, KS-DFT with the same NLPP used in NLPPF, and OF-DFT with BLPSs, as shown in Table II. As expected, the KS-DFT-NLPP and KS-DFT-PAW give almost identical results. Although B_0 of most structures

TABLE II. Relative energy (E_R in eV/atom), bulk modulus (B_0 in GPa), and equilibrium volume (V_0 in Å^3/atom) of Si in various phases obtained by KS-PAW, KS-NLPP, OF-NLPPF, and OF-BLPS. E_R is relative to the CD phase. The mean percentage error (MPE) of V_0 ($\overline{\Delta V_0/V_0^{\rm KS}} = \frac{1}{N}\sum|V_0 - V_0^{\rm KS}|/V_0^{\rm KS}$), mean absolute error (MAE) of E_R ($\overline{\Delta E_R} = \frac{1}{N}\sum|E_R - E_R^{\rm KS}|$), mean percentage error of B_0 ($\overline{\Delta B_0/B_0^{\rm KS}} = \frac{1}{N}\sum|B_0 - B_0^{\rm KS}|/B_0^{\rm KS}$) are listed in last column. The experimental values of V_0 and B_0 for CD-Si are 20.01 Å^3/atom [86] and 99 GPa [84,87,88] at low temperature (77.4 K), respectively.

Si	Method	CD	HD	CBCC	β-tin	BCT5	SC	HCP	BCC	FCC	MPE/MAE
V_0	KS-PAW	20.446	20.427	18.473	15.351	17.614	16.202	14.351	14.638	14.471	
	KS-NLPP	20.438	20.431	18.499	15.398	17.648	16.252	14.436	14.714	14.540	
	OF-BLPS	20.353	20.387	19.235	15.827	17.370	16.120	13.189	12.944	13.283	4.2%
	OF-NLPPF	20.355	20.376	19.319	16.348	17.689	16.552	14.457	14.413	14.516	1.9%
E_R	KS-PAW	0.000	0.011	0.158	0.291	0.288	0.353	0.511	0.524	0.536	
	KS-NLPP	0.000	0.011	0.159	0.292	0.287	0.351	0.510	0.522	0.534	
	OF-BLPS	0.000	0.007	0.057	0.033	−0.193	−0.182	0.101	0.266	0.073	0.279
	OF-NLPPF	0.000	0.005	0.061	0.094	−0.159	−0.152	0.334	0.491	0.306	0.188
B_0	KS-PAW	88.2	88.3	94.8	107.6	94.6	99.9	87.3	92.0	83.4	
	KS-NLPP	86.8	87.2	93.2	106.0	94.2	98.9	87.1	92.7	82.6	
	OF-BLPS	94.7	95.1	101.2	97.8	110.2	106.2	97.9	98.1	101.1	10.4%
	OF-NLPPF	97.4	98.2	104.2	106.5	115.4	114.7	110.8	99.5	111.7	15.4%

obtained by OF-DFT-NLPPF are slightly worse than those obtained by OF-DFT-BLPS, the significant improvements for the V_0 and E_R of most structures are observed using OF-DFT-NLPPF versus OF-DFT-BLPS, as demonstrated by the fact that the mean percentage error of V_0 and mean absolute error of E_R of OF-DFT with NLPPF are 1.9% and 188 meV/atom, respectively, which are smaller than those of 4.2% and 279 meV/atom obtained by OF-DFT with BLPS. Overall, the OF-DFT with NLPPF exhibits reasonable reproductions of bulk properties of crystalline Si obtained by KS-DFT, which are in reasonable agreement with the available experimental values.

Moreover, the bulk properties of crystalline phases of Ge [84,89,90,93] predicted by KS-DFT, using NLPP and PAW formalisms, and by OF-DFT, using the OEPP and NLPPF, are given in Table III. We again observe a marked improvement of bulk properties in the most crystalline phases of Ge, compared with OF-DFT with OEPP. Specifically, the bulk properties (E_R, V_0, and B_0) obtained by KS-DFT are better reproduced by OF-DFT with NLPPF than by OF-DFT with OEPP for most phases of Ge. All of these results reveal that OF-DFT with NLPPF, in general, gives more accurate results than the OF-DFT with LPPs. Particularly, the mean percentage errors of V_0, E_R, and B_0 obtained by OF-DFT with NLPPF are significantly less than those obtained by OF-DFT with BLPS for Ge.

To demonstrate the transferability of NLPPF, we apply it to predict the energy differences for the fifty random structures of Si generated by CALYPSO software [94,95]. Notably, OF-DFT with NLPPF results are closer to KS-DFT results (Fig. 1), in which the average error of energies calculated by NLPPF relative to the KS-DFT energies (268 meV/atom) is smaller than that (429 meV/atom) obtained by the OF-DFT with LPP.

TABLE III. E_R (eV/atom), B_0 (GPa), V_0 (Å^3/atom) of Ge in various phases including CD, β-tin, SC, HCP, BCC, FCC, and two experimental structures with space group of *Imma* [89] and *Cmma* [90] space group obtained by KS-PAW, KS-NLPP, OF-NLPPF, and OF-OEPP. E_R is relative to the CD phase. The mean percentage and absolute errors are also listed as Table II. The experimental values of B_0 and V_0 for CD-Ge are 77 GPa [84,87,91] and 22.626 Å^3/atom [92] at low temperature (77.4 K) and room temperature (298 K), respectively.

Ge	Method	CD	β-tin	*Imma*	SC	*Cmma*	HCP	FCC	BCC	MPE / MAE
V_0	KS-PAW	24.179	19.441	19.419	20.036	19.350	19.434	19.651	19.344	
	KS-NLPP	24.308	19.636	19.616	20.240	19.540	19.570	19.779	19.496	
	OF-OEPP	23.339	19.060	18.885	19.194	18.032	17.656	17.638	18.343	5.4%
	OF-NLPPF	24.234	20.137	19.829	20.055	19.142	18.815	18.769	20.345	2.5%
E_R	KS-PAW	0.000	0.217	0.226	0.233	0.297	0.311	0.312	0.319	
	KS-NLPP	0.000	0.204	0.211	0.223	0.278	0.290	0.289	0.298	
	OF-OEPP	0.000	0.011	−0.040	−0.151	0.125	0.225	0.194	0.359	0.159
	OF-NLPPF	0.000	0.042	−0.001	−0.134	0.224	0.366	0.330	0.450	0.131
B_0	KS-PAW	58.8	69.5	67.7	68.4	66.3	64.3	63.9	65.5	
	KS-NLPP	56.5	68.0	67.4	67.4	65.6	64.1	64.3	65.5	
	OF-OEPP	69.7	82.9	86.8	86.2	82.9	83.5	86.1	67.2	23.1%
	OF-NLPPF	62.2	72.7	73.3	73.5	63.4	58.3	62.1	49.8	8.3%

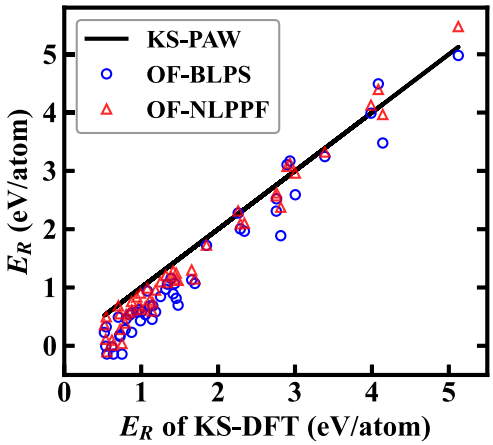

FIG. 1. The E_R obtained by OF-DFT with NLPPF and BLPS are compared with KS-DFT of Si for 50 random structures generated by CALYPSO.

To further benchmark the transferability of the NLPPF scheme, we also calculate the bulk properties of selected Ga and As solids, as well as the binary compound of GaAs. The detailed bulk properties are presented in Tables S1–S3 of the Supplemental Material [71]. The curves of relative energy versus volume equation of state (EOS) for the stable phases of Ga, As, and GaAs (i.e., α-Ga [96], α-As [97], and zincblende GaAs [98]) are calculated and shown in Fig. 2. The OF-DFT calculations using NLPPF yield results in excellent agreement with the KS-DFT results, particularly for GaAs, where the EOS curves calculated by OF-DFT-NLPPF almost coincide with that obtained by KS-DFT, showing no obvious volume difference at any given volumes. In contrast, the EOS curves calculated from OF-DFT with BLPS exhibit significant differences and consistently underestimate the equilibrium volumes compared with KS-DFT results. These findings indicate that if the NLPPF is well suited for describing the elements, it can also perform effectively for compounds composed of these elements.

B. Analysis of the applicability of NLPPF method

Despite OF-DFT with NLPPF giving accurate predictions of the EOS for Ge, it fails to reproduce the properties of carbon with CD structure (Fig. 3). To uncover the physical origin of the deviation, we estimate the errors of the KED and

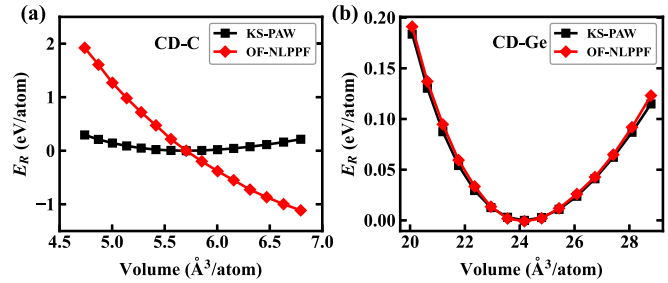

FIG. 3. Relative energy versus volume curves are calculated using KS-DFT (black squares) and OF-DFT with NLPPF (red diamonds) for (a) CD C and (b) CD Ge.

nonlocal electron-ion interaction energy density, denoted by $\epsilon(\mathbf{r}) = \int V_{\rm nl}(\mathbf{r}, \mathbf{r}')\gamma_s(\mathbf{r}', \mathbf{r})d\mathbf{r}'$, obtained by OF-DFT employing revHC KEDF with respect to the KS-DFT along the [111] directions in the diamond structures of C and Ge (Fig. 4). The KED (τ_s) calculated by the revHC-KEDF can accurately reproduce the results of KS-DFT for Ge, whereas the large discrepancies of KED calculated by OF-DFT with revHC-KEDF and KS-DFT exist for C. Therefore, we believe that the bulk properties discrepancies obtained by the framework of OF-DFT within the NLPPF are derived from the errors in the kinetic-energy densities for C. The finding is fairly consistent with our previous work [52].

It is well known that our proposed NLPPF scheme crucially relies on the approximations of MG form of the density matrix [55] functional and the KED [55,99], as manifested by Eqs. (10) and (5). To investigate the role of these approximations, we first evaluate the of $\epsilon^{\rm NLPPF}$ with respect to the $\epsilon^{\rm KS}$ obtained by KS-DFT using the KS-KEDs according to Eq. (10). Our calculations reveal that the difference between $\epsilon^{\rm NLPPF}(\tau_s)$ and the exact $\epsilon^{\rm KS}$ is small for the whole considered region for both C and Ge. These results indicate that the MG form of the density functional proposed in our NLPPF scheme is an appropriate approximation. Once the revHC KED is employed to calculate the ϵ for C according to Eq. (5), it leads to significant deviations of $\epsilon^{\rm NLPPF}(\tau_s^{\rm revHC})$ with respect to the exact $\epsilon^{\rm KS}$, particularly in the near-core region. In contrast, a minor deviation of $\epsilon^{\rm NLPPF}(\tau_s^{\rm revHC})$ from exact $\epsilon^{\rm KS}$ exists for Ge. The results are consistent with our previous finding that the accuracy of NLPPF should depend sensitively on the KED. Since the KED usually can be derived from the KEDF, it can be expected that our proposed NLPPF

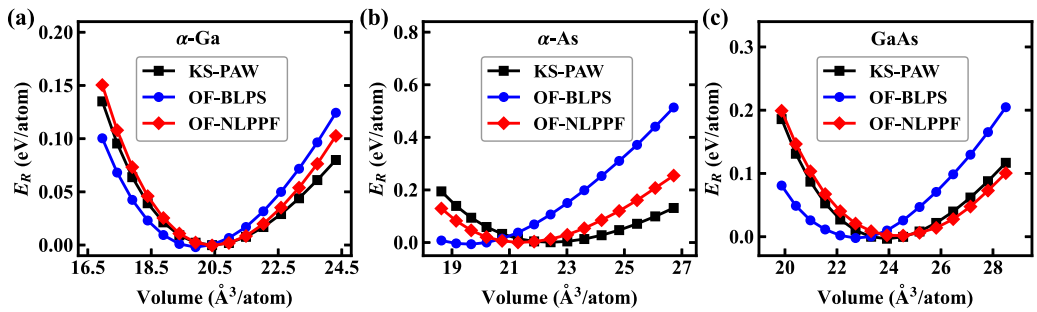

FIG. 2. Relative energy versus volume curves are calculated using KS-DFT (black squares) and OF-DFT with BLPS (blue circles) and NLPPF (red diamonds) for α-Ga (a), α-As (b), and GaAs (c).

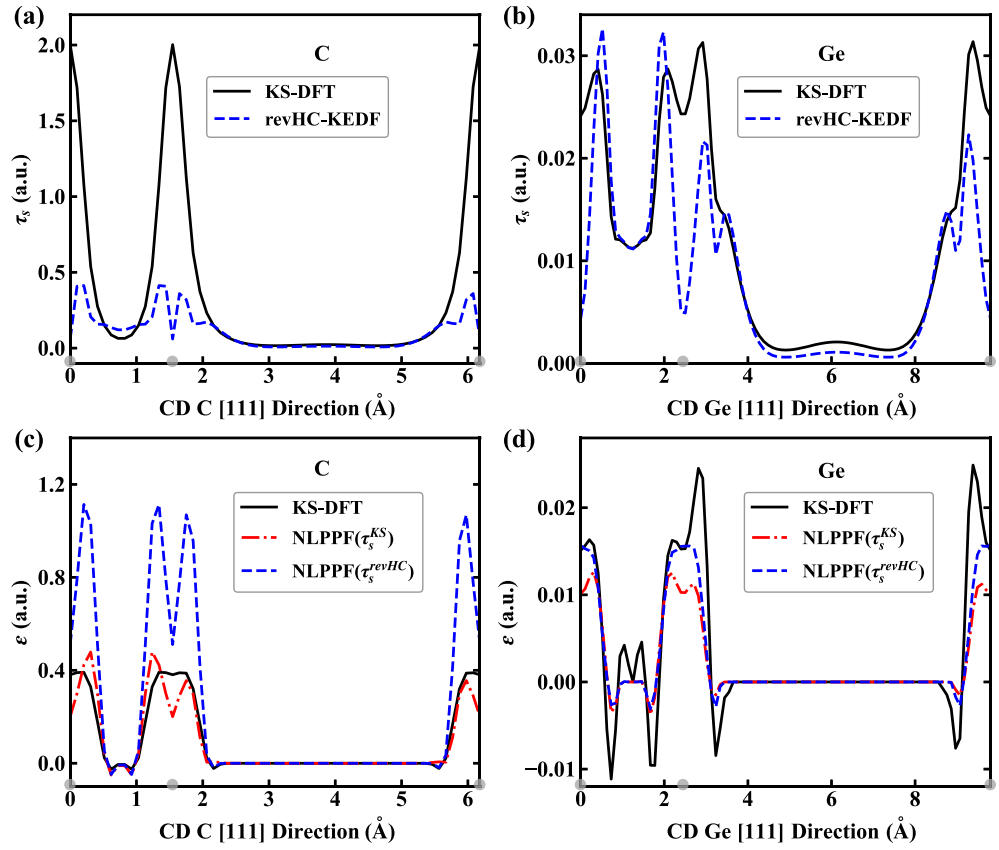

FIG. 4. KED (τ_s) and nonlocal electron-ion interaction energy density (ϵ) were calculated by KS-DFT and OF-DFT for CD C and CD Ge along the [111] direction. The positive-definite KED of KS-DFT ($\tau_s = \sum_i f_i \frac{|\nabla\phi_i|^2}{2}$) was used. Note that i and f_i denote the index of KS orbitals and the occupation number, respectively. The gray points stand for atom position.

is primarily governed by KEDF in OF-DFT. Therefore, it is anticipated that the OF-DFT with NLPPF can be widely applied to the general semiconducting systems once an accurate KEDF is available.

C. Computational cost

To assess the computational efficiency of NLPPF, we performed the single-point energy calculations of CD Si supercells containing 64 to 2744 atoms using OF-DFT with NLPPF and BLPS, respectively. The total wall time required for these calculations using OF-DFT with NLPPF and BLPS is presented in Fig. 5. To make a clean comparison, the total wall time required for KS-DFT calculations with PAW [79] is also presented. Note that all calculations were performed on a node with 2 Intel(R) Xeon(R) Gold 6240R CPUs and 192 GB of RAM. Just as shown in Fig. 5, the total wall time for OF-DFT with NLPPF is around 3.5 times larger than that using OF-DFT with BLPS calculations and the computational cost of OF-DFT with both NLPPF and BLPS clearly scales linearly with the number of atoms in the simulation cell, in sharp contrast to the cubic scaling of KS-DFT. This dramatic reduction of the total wall times of OF-DFT within NLPPF scheme leads us to expect that it holds great promise for simulations of the large-scale semiconducting systems.

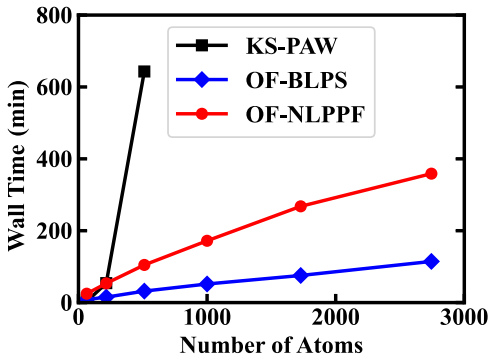

FIG. 5. Wall times of single-point OF-DFT and KS-DFT calculations. The simulations of CD Si supercells containing 64 to 2744 atoms. The OF-DFT calculations are carried out with the NLPPF and BLPS, revHC functional, and OE-SCF solver [74]. The KS-DFT uses the PAW method.

V. CONCLUSIONS

Inherited from NLPPF scheme, an extended NLPPF approach has been proposed by a combination with the revHC KEDF for simulations of semiconductors. We have demonstrated that our proposed NLPPF scheme can successfully reproduce the bulk properties for various semiconducting systems (e.g., Si, Ge, and GaAs), indicating the great

improvement in the computational accuracy and transferability over LPPs. Notably, the new scheme retains linear computational scaling, opening up new avenues for simulations of large-scale semiconductors. It is worthwhile pointing out that the accuracy of NLPPF scheme is largely determined by the quality of KED. Therefore, the challenges remain in accurately simulating systems with localized valence electrons, such as those characterized by $2p$ and $3d$ orbitals, where no accurate KEDF is available.

ACKNOWLEDGMENTS

This research was supported by the National Natural Science Foundation of China under Grants No. T2225013, No. 12047530, No. 12274174, No. 1230050631, No. 12274171, No. 12174142, No. 12034009, and No. 12305002, the Program for JLU Science and Technology Innovative Research Team, and the Science Challenge Project No. TZ2016001. Part of the calculation was performed in the high-performance computing center of Jilin University.

[1] P. Hohenberg and W. Kohn, Inhomogeneous electron gas, Phys. Rev. **136**, B864 (1964).
[2] W. Kohn and L. J. Sham, Self-consistent equations including exchange and correlation effects, Phys. Rev. **140**, A1133 (1965).
[3] M. C. Payne, M. P. Teter, D. C. Allan, T. A. Arias, and J. D. Joannopoulos, Iterative minimization techniques for *ab initio* total-energy calculations: Molecular dynamics and conjugate gradients, Rev. Mod. Phys. **64**, 1045 (1992).
[4] X. Li and H. Gao, Atomistic modelling of deformation and failure mechanisms in nanostructured materials, Natl. Sci. Rev. **2**, 133 (2015).
[5] E. Fermi, Statistical method to determine some properties of atoms, Rend. Accad. Naz. Lincei **6**, 602 (1927).
[6] L. H. Thomas, The calculation of atomic fields, Math. Proc. Cambridge Philos. Soc. **23**, 542 (1927).
[7] C. F. v. Weizsäcker, Zur theorie der kernmassen, Eur. Phys. J. A **96**, 431 (1935).
[8] J. Lindhard, On the properties of a gas of charged particles, K. Dan. Vidensk. Selsk. Mat. Fys. Medd. **28**, 8 (1954).
[9] A. Nagy and N. H. March, The exact form of the Pauli potential for the ground state of two-and three-level atoms and ions, Int. J. Quantum Chem. **39**, 615 (1991).
[10] V. V. Karasiev and S. B. Trickey, Chapter Nine - Frank discussion of the status of ground-state orbital-free DFT, Adv. Quantum Chem. **71**, 221 (2015).
[11] N. H. March, Differential equation for the ground-state density in finite and extended inhomogeneous electron gases, Phys. Lett. A **113**, 66 (1985).
[12] D. I. Palade, Nonlocal orbital-free kinetic pressure tensors for the Fermi gas, Phys. Rev. B **98**, 245401 (2018).
[13] W. Mi, K. Luo, S. B. Trickey, and M. Pavanello, Orbital-free density functional theory: An attractive electronic structure method for large-scale first-principles simulations, Chem. Rev. **123**, 12039 (2023).
[14] W. C. Witt, B. G. Del Rio, J. M. Dieterich, and E. A. Carter, Orbital-free density functional theory for materials research, J. Mater. Res. **33**, 777 (2018).
[15] V. V. Karasiev and S. B. Trickey, Issues and challenges in orbital-free density functional calculations, Comput. Phys. Commun. **183**, 2519 (2012).
[16] W. Mi, X. Shao, C. Su, Y. Zhou, S. Zhang, Q. Li, H. Wang, L. Zhang, M. Miao, Y. Wang, and Y. Ma, ATLAS: A real-space finite-difference implementation of orbital-free density functional theory, Comput. Phys. Commun. **200**, 87 (2016).
[17] L. E. González and D. J. González, Orbital-free ab-initio study of the structure of liquid Al on a model fcc metallic wall: The influence of surface orientation. J. Phys.: Conf. Ser. **98**, 062024 (2008).
[18] A. Aguado, D. J. González, L. E. González, J. M. López, S. Núnez, and M. J. Stott, An orbital free *ab initio* method: Applications to liquid metals and clusters, in *Recent Progress in Orbital-Free Density Functional Theory* (World Scientific, Singapore, 2013), pp. 55–145.
[19] M. Chen, J. Xia, C. Huang, J. M. Dieterich, L. Hung, I. Shin, and E. A. Carter, Introducing PROFESS 3.0: An advanced program for orbital-free density functional theory molecular dynamics simulations, Comput. Phys. Commun. **190**, 228 (2015).
[20] J. J. Mortensen, L. B. Hansen, and K. W. Jacobsen, Real-space grid implementation of the projector augmented wave method, Phys. Rev. B **71**, 035109 (2005).
[21] S. Das, P. Motamarri, V. Subramanian, D. M. Rogers, and V. Gavini, DFT-FE 1.0: A massively parallel hybrid CPU-GPU density functional theory code using finite-element discretization, Comput. Phys. Commun. **280**, 108473 (2022).
[22] X. Shao, K. Jiang, W. Mi, A. Genova, and M. Pavanello, DFTpy: An efficient and object-oriented platform for orbital-free DFT simulations, Wiley Interdiscip. Rev. Comput. Mol. Sci. **11**, e1482 (2021).
[23] P. Golub and S. Manzhos, CONUNDrum: A program for orbital-free density functional theory calculations, Comput. Phys. Commun. **256**, 107365 (2020).
[24] X. Shao, Q. Xu, S. Wang, J. Lv, Y. Wang, and Y. Ma, Large-scale *ab initio* simulations for periodic system, Comput. Phys. Commun. **233**, 78 (2018).
[25] L. Hung and E. A. Carter, Accurate simulations of metals at the mesoscale: Explicit treatment of 1 million atoms with quantum mechanics, Chem. Phys. Lett. **475**, 163 (2009).
[26] M. Chen, X.-W. Jiang, H. Zhuang, L.-W. Wang, and E. A. Carter, Petascale orbital-free density functional theory enabled by small-box algorithms, J. Chem. Theory Comput. **12**, 2950 (2016).
[27] E. Chacón, J. Alvarellos, and P. Tarazona, Nonlocal kinetic energy functional for nonhomogeneous electron systems, Phys. Rev. B **32**, 7868 (1985).
[28] L.-W. Wang and M. P. Teter, Kinetic-energy functional of the electron density, Phys. Rev. B **45**, 13196 (1992).
[29] E. Smargiassi and P. A. Madden, Orbital-free kinetic-energy functionals for first-principles molecular dynamics, Phys. Rev. B **49**, 5220 (1994).

[30] F. Perrot, Hydrogen-hydrogen interaction in an electron gas, J. Phys.: Condens. Matter **6**, 431 (1994).
[31] Y. A. Wang, N. Govind, and E. A. Carter, Orbital-free kinetic-energy functionals for the nearly free electron gas, Phys. Rev. B **58**, 13465 (1998).
[32] Y. A. Wang, N. Govind, and E. A. Carter, Orbital-free kinetic-energy density functionals with a density-dependent kernel, Phys. Rev. B **60**, 16350 (1999).
[33] Q. Xu, Y. Wang, and Y. Ma, Nonlocal kinetic energy density functional via line integrals and its application to orbital-free density functional theory, Phys. Rev. B **100**, 205132 (2019).
[34] W. Mi, A. Genova, and M. Pavanello, Nonlocal kinetic energy functionals by functional integration, J. Chem. Phys. **148**, 184107 (2018).
[35] C. Huang and E. A. Carter, Nonlocal orbital-free kinetic energy density functional for semiconductors, Phys. Rev. B **81**, 045206 (2010).
[36] Q. Xu, J. Lv, Y. Wang, and Y. Ma, Nonlocal kinetic energy density functionals for isolated systems obtained via local density approximation kernels, Phys. Rev. B **101**, 045110 (2020).
[37] X. Shao, W. Mi, and M. Pavanello, Revised Huang-Carter nonlocal kinetic energy functional for semiconductors and their surfaces, Phys. Rev. B **104**, 045118 (2021).
[38] K. Luo, V. V. Karasiev, and S. Trickey, A simple generalized gradient approximation for the noninteracting kinetic energy density functional, Phys. Rev. B **98**, 041111(R) (2018).
[39] L. A. Constantin, E. Fabiano, and F. Della Sala, Semilocal Pauli-Gaussian kinetic functionals for orbital-free density functional theory calculations of solids, J. Phys. Chem. Lett. **9**, 4385 (2018).
[40] V. V. Karasiev, D. Chakraborty, O. A. Shukruto, and S. B. Trickey, Nonempirical generalized gradient approximation free-energy functional for orbital-free simulations, Phys. Rev. B **88**, 161108(R) (2013).
[41] J. Xia, C. Huang, I. Shin, and E. A. Carter, Can orbital-free density functional theory simulate molecules?, J. Chem. Phys. **136**, 084102 (2012).
[42] W. Mi and M. Pavanello, Orbital-free density functional theory correctly models quantum dots when asymptotics, nonlocality, and nonhomogeneity are accounted for, Phys. Rev. B **100**, 041105(R) (2019).
[43] B. Zhou, Y. Alexander Wang, and E. A. Carter, Transferable local pseudopotentials derived via inversion of the Kohn-Sham equations in a bulk environment, Phys. Rev. B **69**, 125109 (2004).
[44] C. Huang and E. A. Carter, Transferable local pseudopotentials for magnesium, aluminum and silicon, Phys. Chem. Chem. Phys. **10**, 7109 (2008).
[45] W. Mi, S. Zhang, Y. Wang, Y. Ma, and M. Miao, First-principle optimal local pseudopotentials construction via optimized effective potential method, J. Chem. Phys. **144**, 134108 (2016).
[46] B. G. del Rio, J. M. Dieterich, and E. A. Carter, Globally-optimized local pseudopotentials for (orbital-free) density functional theory simulations of liquids and solids, J. Chem. Theory Comput. **13**, 3684 (2017).
[47] L. Goodwin, R. J. Needs, and V. Heine, A pseudopotential total energy study of impurity-promoted intergranular embrittlement, J. Phys.: Condens. Matter **2**, 351 (1990).
[48] V. Heine and I. Abarenkov, A new method for the electronic structure of metals, Philos. Mag. **9**, 451 (1964).
[49] V. V. Karasiev, T. Sjostrom, and S. B. Trickey, Generalized-gradient-approximation noninteracting free-energy functionals for orbital-free density functional calculations, Phys. Rev. B **86**, 115101 (2012).
[50] Y. Ke, F. Libisch, J. Xia, L.-W. Wang, and E. A. Carter, Angular-momentum-dependent orbital-free density functional theory, Phys. Rev. Lett. **111**, 066402 (2013).
[51] Y. Ke, F. Libisch, J. Xia, and E. A. Carter, Angular momentum dependent orbital-free density functional theory: Formulation and implementation, Phys. Rev. B **89**, 155112 (2014).
[52] Q. Xu, C. Ma, W. Mi, Y. Wang, and Y. Ma, Nonlocal pseudopotential energy density functional for orbital-free density functional theory, Nat. Commun. **13**, 1385 (2022).
[53] L. Kleinman and D. M. Bylander, Efficacious form for model pseudopotentials, Phys. Rev. Lett. **48**, 1425 (1982).
[54] D. R. Hamann, M. Schlüter, and C. Chiang, Norm-conserving pseudopotentials, Phys. Rev. Lett. **43**, 1494 (1979).
[55] C. Lee and R. G. Parr, Gaussian and other approximations to the first-order density matrix of electronic systems, and the derivation of various local-density-functional theories, Phys. Rev. A **35**, 2377 (1987).
[56] R. G. Parr and W. Yang, *Density Functional Theory of Atoms and Molecules* (Oxford University Press, New York, 1989).
[57] S. K. Ghosh, M. Berkowitz, and R. G. Parr, Transcription of ground-state density-functional theory into a local thermodynamics., Proc. Natl. Acad. Sci. USA **81**, 8028 (1984).
[58] J. Xia and E. A. Carter, Single-point kinetic energy density functionals: A pointwise kinetic energy density analysis and numerical convergence investigation, Phys. Rev. B **91**, 045124 (2015).
[59] M. Bernasconi, G. L. Chiarotti, and E. Tosatti, Ab initio calculations of structural and electronic properties of gallium solid-state phases, Phys. Rev. B **52**, 9988 (1995).
[60] L. Bosio, A. Defrain, H. Curien, and A. Rimsky, Structure cristalline du gallium β, Acta Cryst. **B25**, 995 (1969).
[61] C. E. Weir, G. J. Piermarini, and S. Block, On the crystal structures of Cs II and Ga II, J. Chem. Phys. **54**, 2768 (1971).
[62] R. W. G. Wyckoff, *Crystal Structures* (Wiley, New York, 1963), Vol. 1, p. 22.
[63] K. R. Lyall and J. F. Cochran, Velocity of sound and acoustic attenuation in pure gallium single crystals, Can. J. Phys. **49**, 1075 (1971).
[64] L. F. Mattheiss, D. R. Hamann, and W. Weber, Structural calculations for bulk As, Phys. Rev. B **34**, 2190 (1986).
[65] B. Morosin and J. E. Schirber, Linear compressibilities and the pressure dependence of the atomic positional parameter of As, Solid State Commun. **10**, 249 (1972).
[66] J. S. Blakemore, Semiconducting and other major properties of gallium arsenide, J. Appl. Phys. **53**, R123 (1982).
[67] C. W. Garland and K. C. Park, Low-temperature elastic constants of gallium arsenide, J. Appl. Phys. **33**, 759 (1962).
[68] B. Svane, K. Tolborg, K. Kato, and B. B. Iversen, Multipole electron densities and structural parameters from synchrotron powder x-ray diffraction data obtained with a MYTHEN detector system (OHGI), Acta Cryst. **A77**, 85 (2021).
[69] H. J. McSkimin and P. Andreatch, Jr., Elastic moduli of diamond as a function of pressure and temperature, J. Appl. Phys. **43**, 2944 (1972).

[70] J. P. Perdew and A. Zunger, Self-interaction correction to density-functional approximations for many-electron systems, Phys. Rev. B **23**, 5048 (1981).

[71] See Supplemental Material at http://link.aps.org/supplemental/10.1103/PhysRevB.109.075144 for derivation of the nonlocal term for HC and revHC KEDFs; functional derivative of NLPPF; detailed bulk properties of Ga, As, GaAs, and C; bulk properties of Si with local density approximation exchange-correlation; and PAW potentials used in this work. The Supplemental Material also contains Refs. [59–70].

[72] N. Troullier and J. L. Martins, Efficient pseudopotentials for plane-wave calculations, Phys. Rev. B **43**, 1993 (1991).

[73] M. Fuchs and M. Scheffler, Ab initio pseudopotentials for electronic structure calculations of poly-atomic systems using density-functional theory, Comput. Phys. Commun. **119**, 67 (1999).

[74] X. Shao, W. Mi, and M. Pavanello, Efficient DFT solver for nanoscale simulations and beyond, J. Phys. Chem. Lett. **12**, 4134 (2021).

[75] G. Kresse and J. Furthmüller, Efficient iterative schemes for *ab initio* total-energy calculations using a plane-wave basis set, Phys. Rev. B **54**, 11169 (1996).

[76] G. Kresse and J. Furthmüller, Efficiency of ab-initio total energy calculations for metals and semiconductors using a plane-wave basis set, Comput. Mater. Sci. **6**, 15 (1996).

[77] S. J. Clark, M. D. Segall, C. J. Pickard, P. J. Hasnip, M. I. J. Probert, K. Refson, and M. C. Payne, First principles methods using CASTEP, Z. Krist. Cryst. Mater. **220**, 567 (2005).

[78] Q. Xu, S. Wang, L. Xue, X. Shao, P. Gao, J. Lv, Y. Wang, and Y. Ma, Ab initio electronic structure calculations using a real-space Chebyshev-filtered subspace iteration method, J. Phys.: Condens. Matter **31**, 455901 (2019).

[79] P. E. Blöchl, Projector augmented-wave method, Phys. Rev. B **50**, 17953 (1994).

[80] H. J. Monkhorst and J. D. Pack, Special points for Brillouin-zone integrations, Phys. Rev. B **13**, 5188 (1976).

[81] J. P. Perdew, K. Burke, and M. Ernzerhof, Generalized gradient approximation made simple, Phys. Rev. Lett. **77**, 3865 (1996).

[82] J. P. Perdew, K. Burke, and M. Ernzerhof, Generalized gradient approximation made simple, Phys. Rev. Lett. **78**, 1396(E) (1997).

[83] L. L. Boyer, E. Kaxiras, J. L. Feldman, J. Q. Broughton, and M. J. Mehl, New low-energy crystal structure for silicon, Phys. Rev. Lett. **67**, 715 (1991).

[84] M. T. Yin and M. L. Cohen, Theory of static structural properties, crystal stability, and phase transformations: Application to Si and Ge, Phys. Rev. B **26**, 5668 (1982).

[85] F. D. Murnaghan, The compressibility of media under extreme pressures, Proc. Natl. Acad. Sci. USA **30**, 244 (1944).

[86] D. N. Batchelder and R. O. Simmons, Lattice constants and thermal expansivities of silicon and of calcium fluoride between 6° and 322°K, J. Chem. Phys. **41**, 2324 (1964).

[87] H. J. McSkimin, Measurement of elastic constants at low temperatures by means of ultrasonic waves–data for silicon and germanium single crystals, and for fused silica, J. Appl. Phys. **24**, 988 (1953).

[88] H. J. McSkimin and P. Andreatch, Jr., Elastic moduli of silicon vs hydrostatic pressure at 25.0 °C and −195.8 °C, J. Appl. Phys. **35**, 2161 (1964).

[89] R. J. Nelmes, H. Liu, S. A. Belmonte, J. S. Loveday, M. I. McMahon, D. R. Allan, D. Häusermann, and M. Hanfland, Imma phase of germanium at ∼80 GPa, Phys. Rev. B **53**, R2907(R) (1996).

[90] K. Takemura, U. Schwarz, K. Syassen, M. Hanfland, N. E. Christensen, D. L. Novikov, and I. Loa, High-pressure *Cmca* and hcp phases of germanium, Phys. Rev. B **62**, R10603(R) (2000).

[91] H. J. McSkimin and P. Andreatch, Jr., Elastic moduli of germanium versus hydrostatic pressure at 25.0 °C and −195.8° C, J. Appl. Phys. **34**, 651 (1963).

[92] A. S. Cooper, Precise lattice constants of germanium, aluminum, gallium arsenide, uranium, sulphur, quartz and sapphire, Acta Cryst. **15**, 578 (1962).

[93] S. B. Qadri, E. F. Skelton, and A. W. Webb, High pressure studies of Ge using synchrotron radiation, J. Appl. Phys. **54**, 3609 (1983).

[94] Y. Wang, J. Lv, L. Zhu, and Y. Ma, Crystal structure prediction via particle-swarm optimization, Phys. Rev. B **82**, 094116 (2010).

[95] Y. Wang, J. Lv, L. Zhu, and Y. Ma, CALYPSO: A method for crystal structure prediction, Comput. Phys. Commun. **183**, 2063 (2012).

[96] A. J. Bradley, The crystal structure of gallium, Z. Krist. Cryst. Mater. **91**, 302 (1935).

[97] D. Schiferl and C. S. Barrett, The crystal structure of arsenic at 4.2, 78 and 299 °K, J. Appl. Cryst. **2**, 30 (1969).

[98] A. W. Stevenson, Thermal vibrations and bonding in GaAs: An extended-face crystal study, Acta Cryst. **A50**, 621 (1994).

[99] M. Berkowitz, Exponential approximation for the density matrix and the Wigner's distribution, Chem. Phys. Lett. **129**, 486 (1986).